

The classical flipping ratio technique applied to non classical magnetic materials: Molecule-based and Photoswitchable magnetic compounds

B. Gillon¹

¹ Laboratoire Léon Brillouin (CEA-CNRS), CE Saclay, 91191 Gif-sur-Yvette, France

Abstract. Applications of the classical flipping ratio technique to the determination of the spin density by polarised neutron diffraction (PND) are described. In the domain of molecule-based magnetic compounds, such investigations provide direct information on the nature and the origin of the intra- and inter-molecular magnetic interactions. For instance, the visualisation of the spin distribution in the crystal cell and in the molecule enables to demonstrate the interaction pathways between the magnetic centres (transition metals ions, organic radicals) and to investigate the role of the spin delocalisation and spin polarisation effects in the interaction mechanisms. Moreover, the experimental spin density in large molecular clusters permits to elucidate the nature of the magnetic ground state that results from the competition between antiferromagnetic intramolecular interactions. Photomagnetism in molecule-based compounds receives a growing interest, because of the possible future applications of photo-switchable magnetic materials. Spin crossover compounds containing an octahedrally coordinated Fe^{2+} ion present a low spin diamagnetic ($S = 0$) ground state which can be switched, under light illumination with a suitable light wavelength, to a high spin paramagnetic ($S = 2$) metastable state having an extremely long lifetime at low temperature. The magnetisation density in a photoexcited magnetic state was determined for the first time for the spin crossover complex $[\text{Fe}^{\text{II}}(\text{ptz})_6](\text{BF}_4)_2$ (ptz = 1-propyltetrazole).

1 INTRODUCTION

This chapter is devoted to applications of the classical flipping ratio technique to spin density studies in magnetic materials, which are ‘non classical’ because of their molecular character, in contrast with usual intermetallic transition metal or rare earth magnetic compounds. Some of these molecule-based materials moreover display unusual properties like photo-magnetism, i.e. magnetism induced by irradiation with light of suitable wavelength.

Molecule-based magnetic materials [1] can be either molecular crystals, in which magnetic interactions between molecules may lead to magnetic ordering, or extended crystalline networks formed by assembling transition metal ions with molecular precursors, which may show spontaneous magnetisation at room temperature like the Prussian blue derivative $\text{V}_3^{\text{II}}[\text{Cr}^{\text{III}}(\text{CN})_6]_2 \cdot n\text{H}_2\text{O}$ [2]. A large variety of magnetic behaviours can be found in systems where transition metal ions are coupled through organic bridges. For example, magnetic molecular clusters, which constitute single molecule magnets of nanometre size, may present both quantum and classical magnetic behaviours, because their size is intermediate between simple paramagnetic molecules and a bulk material [3].

In this chapter, the principles of the classical flipping ratio technique will be first recalled. Then the different methods for analysing the data in order to reconstruct the magnetisation density from the flipping ratio measurements will be presented.

Basic concepts concerning the magnetic interaction mechanisms in molecule-based compounds will be introduced. Spin density studies give access to crucial information about the main interaction processes because they permit to determine the distribution of the magnetic moments on the molecule (spin delocalisation effect), the sign of the spin density (spin polarisation effect) and the shape of the atomic densities (accidental orthogonality) [4].

In order to illustrate the interest of such investigations, several examples will be given for compounds exhibiting various magnetic behaviours. A first part will concern systems in which the magnetism arises from $2p$ unpaired electrons of organic radicals; in a second part, investigations of systems including interacting transition metal ions will be reported.

Finally the first determination of the magnetisation density in a photo-excited state of a spin crossover Fe^{II} complex will be described.

2 CLASSICAL FLIPPING RATIO TECHNIQUE

The classical flipping ratio technique consists in measuring flipping ratios of a set of Bragg reflections by diffraction of a polarised neutron beam on a single crystal on a two axes polarised neutron diffractometer in order to get an experimental determination of the magnetic structure factors.

The diffractometer 5C1 of the LLB is a conventional two-axis polarised neutron diffractometer, with a lifting counter, installed on the hot source of the Orphée reactor (Figure 1). Two other diffractometers of the same type, but with different technical characteristics are implemented in Grenoble at the ILL: D3 on the hot source and D23 on a thermal guide.

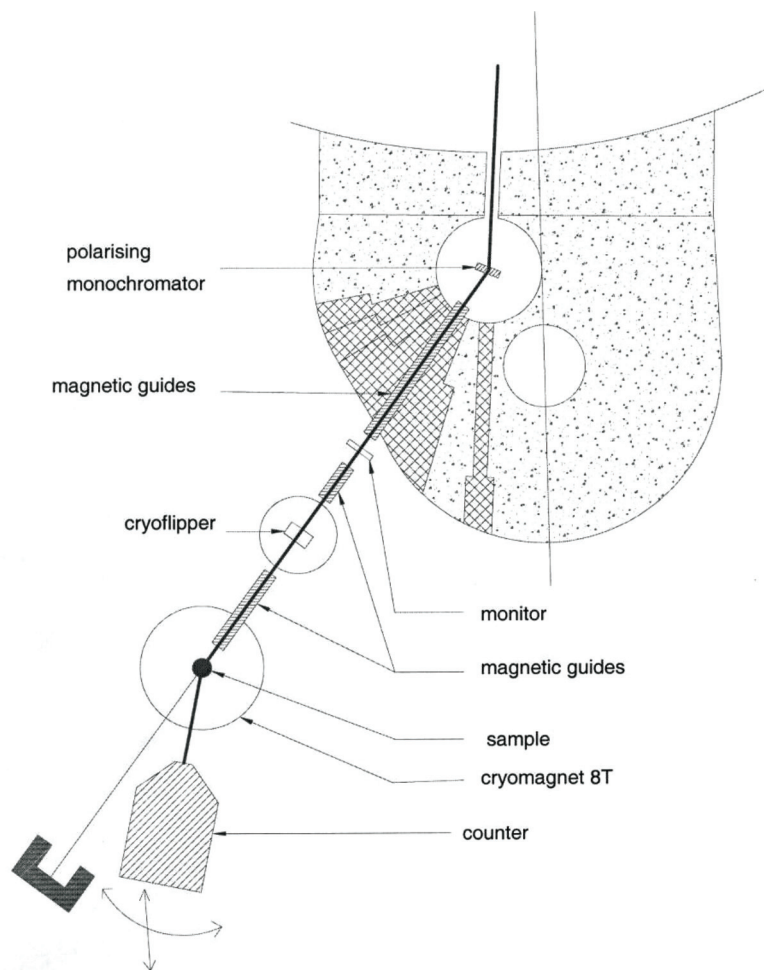


Figure 1. The polarised neutron diffractometer 5C1 at the LLB.

On the 5C1 diffractometer, the polarised monochromatic neutron beam is obtained by diffraction on a Heusler Cu_2MnAl ferromagnetic single crystal, using the (111) reflection in transmission geometry. The monochromator is placed in a static field of 0.4 Tesla of a permanent magnet. The wavelength of 0.84 Å, which corresponds to the maximum of flux of the hot source, allows the investigation of a

large domain of the reciprocal space. A polarisation of the neutron beam of 90 per cent is achieved. The polarisation direction of the incident neutrons is guided by permanent magnetic guide fields of 200 Gauss and can be inverted alternatively with help of a cryogenic flipping device. An Erbium filter is used to suppress the $\lambda/2$ contamination. A superconducting cryomagnet is available for the sample, with a magnetic field up to 8 Tesla and working temperatures down to 1.5 K. The lifting counter gives access to a vertical angular range from -5 to 20 degrees. An interactive piloting program runs in the Windows NT system on a PC.

The sample is a single crystal, which is placed in a vertical magnetic field in order to align the electronic magnetic moments. Usually a strong magnetic field of several Tesla is needed to induce a strong magnetic response for paramagnetic crystals. In the case of ferromagnetic compounds, a weaker field is sufficient to align the magnetic domains but a minimum field of 0.5 Tesla is required on 5C1 in order to maintain the neutron beam polarisation along its trajectory.

2.1 Principles

The differential cross sections for a polarised neutron beam scattered by a single crystal on a Bragg peak of scattering vector \mathbf{Q} are written in term of the nuclear and magnetic structure factors:

$$\left(\frac{d\sigma}{d\Omega}\right)^{\pm\pm} \propto |F_N \pm F_M^{\perp z}|^2 \quad (2.1)$$

$$\left(\frac{d\sigma}{d\Omega}\right)^{\pm\mp} \propto |F_M^{\perp x} \pm iF_M^{\perp y}|^2 \quad (2.2)$$

where $F_N(\mathbf{Q})$ is the nuclear structure factor:

$$F_N(\mathbf{Q}) = \sum_i^{atoms} b_i e^{i\mathbf{Q}\cdot\mathbf{r}_i} e^{-W_i} \quad (2.3)$$

b_i being the scattering length of atom i , characteristic of the chemical element, and W_i a term accounting for thermal vibrations of the nuclei.

$\mathbf{F}_M(\mathbf{Q})$ is the magnetic structure factor, which is a vector, Fourier component of the magnetisation distribution $\mathbf{M}(\mathbf{r})$:

$$\mathbf{F}_M(\mathbf{Q}) = \int_{unit\ cell} \mathbf{M}(\mathbf{r}) e^{i\mathbf{Q}\cdot\mathbf{r}} d\mathbf{r} \quad (2.4)$$

As no polarisation analysis is performed, the intensities diffracted by the sample, for the up or down incident polarisation directions respectively, are the sums:

$$I_+ = \left(\frac{d\sigma}{d\Omega}\right)^{++} + \left(\frac{d\sigma}{d\Omega}\right)^{+-} \quad (2.5)$$

$$I_- = \left(\frac{d\sigma}{d\Omega}\right)^{-+} + \left(\frac{d\sigma}{d\Omega}\right)^{--} \quad (2.6)$$

which leads to the expression:

$$I(\mathbf{Q})_{\pm} \propto \left[F_N^2 \pm (F_N^* F_M^{\perp z} + F_N F_M^{\perp z*}) + F_M^{\perp 2} \right] \quad (2.7)$$

The vector F_M^{\perp} is the component of the magnetic structure factor perpendicular to the scattering vector \mathbf{Q} and the term $F_M^{\perp z}$ which appears in expressions (2.1), (2.2) and (2.7) is its vertical component (parallel to field), as schematised in Figure 2. It can be written as:

$$F_M^{\perp z} = qF_M^{\perp} = q^2 F_M \quad (2.8)$$

where $q = \sin \alpha$, α being the angle between the scattering vector \mathbf{Q} and the direction of the magnetic structure factor $\mathbf{F}_M(\mathbf{Q})$.

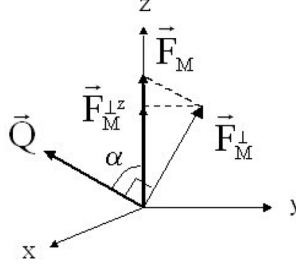


Figure 2. Geometrical definition of the $F_M^{\perp z}$ component.

The following expression of the intensities is obtained using (2.8):

$$I(\mathbf{Q})_{\pm} \propto [F_N^2 \pm q^2(F_N^* F_M + F_N F_M^*) + q^2 F_M^2] \quad (2.9)$$

The flipping ratio of a Bragg reflection is the ratio between the diffracted intensities:

$$R(\mathbf{Q}) = \frac{I_+}{I_-} \quad (2.10)$$

The advantage of measuring such a ratio is that there is no need to measure integrated intensities. The experimental determination of the flipping ratio consists in measuring the peak intensity and the left and right backgrounds in the two incident polarisation cases:

$$R(\mathbf{Q}) = \frac{(\text{peak} - \text{background})_+}{(\text{peak} - \text{background})_-} \quad (2.11)$$

Corrections due to the neutron beam

In the theoretical expression of the flipping ratio deduced from (2.9) and (2.10), corrections are introduced for partial beam polarisation P and flipping efficiency e :

$$P = \frac{n_+ + n_-}{n_+ - n_-} \quad (2.12)$$

The expression of the flipping ratio becomes:

$$R(\mathbf{Q}) = \frac{F_N^2 + Pq^2(F_N^* F_M + F_N F_M^*) + q^2 F_M^2}{F_N^2 - Peq^2(F_N^* F_M + F_N F_M^*) + q^2 F_M^2} \quad (2.13)$$

A third correction related to the neutron beam is applied to take into account the $\lambda/2$ contamination of the incident beam, resulting in an additional term $C_+(\lambda/2)$ in the numerator and $C_-(\lambda/2)$ in the denominator in expression (2.13).

Corrections due to the sample

Other corrections are due to the sample itself. In the case of a sample with strong anisotropic magnetic moments, beam depolarisation by the sample surface may occur and the polarisation has to be corrected using a factor determined by measuring the polarisation before and after the crystal. No absorption

corrections on the intensities are necessary but extinction acts differently on I_+ and I_- . The reduction y_{\pm} of intensity due to extinction depends on the diffracting power σ_{\pm} , which differs whether the incident beam polarisation is up or down [5]:

$$R_{ext} = R \left(\frac{y_+}{y_-} \right) \quad (2.14)$$

Crystals of molecule-based materials don't generally present strong extinction effects, which can then be neglected.

Contributions due to nuclear polarisation and to the Schwinger effect

In the preceding expressions of the cross sections (2.1) and (2.2), only the spin-independent nuclear interaction and the magnetic dipolar interaction between the neutrons magnetic moments and the magnetic field created by the unpaired electron magnetic moments in the sample were considered.

There are actually two other interactions, which give rise to supplementary terms in the cross section:

- The coupling between the neutron spin σ and the nuclear spin \mathbf{I}_i corresponding to the spin dependent part of the nuclear interaction operator:

$$\hat{b}_i = b_i + B_i \mathbf{I}_i \sigma \quad (2.15)$$

where :

$$B_i = \frac{1}{2I_i + 1} (b_i^+ - b_i^-) \quad (2.16)$$

The coefficient B_i is particularly large for hydrogen and therefore the contribution due to the polarisation of the hydrogen nuclear spin by a high magnetic field at low temperature can be non negligible in the case of organic or organometallic molecular compounds due to the large number of H atoms in the cell. The nuclear polarisation structure factor is expressed by:

$$F_{NP}(\mathbf{Q}) = \sum_i^{\text{H atoms}} f_{NP}^i e^{i\mathbf{Q} \cdot \mathbf{r}_i} \quad (2.17)$$

where the polarisation coefficient f_{NP}^i is equal to:

$$f_{NP}^i = 14.89 \times 10^{-4} \frac{\text{H(Tesla)}}{\text{T(K)}} (10^{-12} \text{ cm}) \quad (2.18)$$

- The interaction between the neutron magnetic moments and the electric field due to electrons and nuclei in the sample [6]: this effect is called the Schwinger effect. The Schwinger structure factor ($A_S + iB_S$) is calculated using the charge form factors [7,8].

2.2 Centric case

For centric structures, both nuclear and magnetic structure factors are real and the expression (2.13) of the flipping ratio becomes:

$$R(\mathbf{Q}) = \frac{F_N^2 + 2Pq^2 F_N F_M + q^2 F_M^2}{F_N^2 - 2Peq^2 F_N F_M + q^2 F_M^2} \quad (2.19)$$

The measurement of the experimental flipping ratio R_{exp} permits to write a second order equation:

$$\gamma^2 + B\gamma + C = 0 \quad (2.20)$$

with variable:

$$\gamma = \left(\frac{F_M}{F_N} \right) \quad (2.21)$$

and coefficients B and C which are known from the experimental data:

$$B = -2P \left(\frac{R_{\text{exp}} e + 1}{R_{\text{exp}} - 1} \right) \quad (2.22)$$

$$C = \frac{1}{q^2} \quad (2.23)$$

This second order equation has generally only one physically meaningful root yielding the experimental value of the ratio γ^{exp} between the magnetic and nuclear structure factors. The value of $F_N(\mathbf{Q})$ is deduced either from the low temperature nuclear structure or from the experimental nuclear intensity $\sqrt{F_N^2}$ with the theoretical sign. The magnetic structure factor is then given by:

$$F_M^{\text{exp}} = \gamma^{\text{exp}} F_N \quad (2.24)$$

Contribution due to hydrogen nuclear polarisation

This term $F_{\text{NP}}(\mathbf{Q})$ is spin dependent and the scattering cross-section (2.7) becomes in the centric case:

$$I(\mathbf{Q})_{\pm} \propto \left[F_N^2 \pm 2F_N(F_M^{\perp z} + F_{\text{NP}}) + F_M^{\perp 2} + F_{\text{NP}}^2 + 2F_M^{\perp} F_{\text{NP}} \right] \quad (2.25)$$

The flipping ratio can be written as:

$$R(\mathbf{Q}) = \frac{F_N^2 + 2PF_N(q^2 F_M + F_{\text{NP}}) + q^2 F_M^2 + F_{\text{NP}}^2 + 2qF_M F_{\text{NP}}}{F_N^2 - 2PeF_N(q^2 F_M + F_{\text{NP}}) + q^2 F_M^2 + F_{\text{NP}}^2 + 2qF_M F_{\text{NP}}} \quad (2.26)$$

The coefficients of the second order equation (2.20) have then to be replaced by:

$$B = -2P \left(\frac{R_{\text{exp}} e + 1}{R_{\text{exp}} - 1} \right) + 2 \left(\frac{F_{\text{NP}}}{F_N} \right) \quad (2.27)$$

$$C = \frac{1}{q^2} - \frac{2P}{q^2} \left(\frac{R_{\text{exp}} e + 1}{R_{\text{exp}} - 1} \right) \frac{F_{\text{NP}}}{F_N} + \frac{1}{q^2} \left(\frac{F_{\text{NP}}}{F_N} \right)^2 \quad (2.28)$$

Orbital contribution

The magnetisation density (in magnitude) is the sum of a pure spin contribution and an orbital contribution due to the interaction between the neutron magnetic moment and the magnetic field created by the unpaired electrons moving on their orbits.

$$M(\mathbf{r}) = \rho_S(\mathbf{r}) + \rho_L(\mathbf{r}) \quad (2.29)$$

The magnitude of magnetic structure factor is then the sum of two contributions:

$$F_M(\mathbf{Q}) = F_M^S(\mathbf{Q}) + F_M^L(\mathbf{Q}) \quad (2.30)$$

For organic radicals, the unpaired electron moves on a $2p$ orbital and the orbital moment is quenched. Therefore the magnetisation density is identical to the spin density. For metal-containing systems, the orbital contribution has to be taken into account, except in the case of systems with zero angular momentum like the Mn^{2+} ion with half filled $3d$ shell ($3d^5$, $e_g^2 t_{2g}^3$, $S = 5/2$) or the Cr^{3+} ion ($3d^3$, t_{2g}^3 , $S = 3/2$). However for most of the transition metals ions, the spin-orbit coupling is much smaller than the crystal field and the orbital moment is almost entirely quenched. The orbital contribution can be neglected or treated as a correction using the dipolar approximation [9]:

$$F_M^L(\mathbf{Q}) = m_s \frac{(g-2)}{g} (\langle j_0 \rangle + \langle j_2 \rangle) \quad (2.31)$$

where m_s is the magnetic moment associated with spin, g is the Landé splitting factor and $\langle j_0 \rangle$, $\langle j_2 \rangle$ are radial integrals, Fourier transform of the radial functions with help of the spherical Bessel functions of order 0 and 2 respectively [10].

The pure spin contribution to the magnetic structure factor is then deduced from the experimental magnetic structure factor by:

$$F_M^S(\mathbf{Q}) = F_M^{\text{exp}}(\mathbf{Q}) - F_M^L(\mathbf{Q}) \quad (2.32)$$

2.3 Non centric case

In the case of a non centric space group, both nuclear and magnetic structure factors are complex quantities with real parts A_N , A_M and imaginary parts B_N , B_M . The expression (2.13) of the flipping ratio becomes:

$$R(\mathbf{Q}) = \frac{A_N^2 + B_N^2 + 2Pq^2(A_N A_M + B_N B_M) + q^2(A_M^2 + B_M^2)}{A_N^2 + B_N^2 - 2Peq^2(A_N A_M + B_N B_M) + q^2(A_M^2 + B_M^2)} \quad (2.33)$$

At the difference to the centric case, it is not possible to deduce the two unknown quantities A_M and B_M from one flipping ratio measurement. To overcome this difficulty, a model refinement of the spin density was adapted in order to fit the calculated flipping ratios on the basis of experimental ones [11]. All the corrections have to be introduced directly in expression (2.33). The general expression of the flipping ratio in the non centric case taking into account the structure factors for nuclear polarisation ($A_{PN} + iB_{PN}$) and Schwinger effect ($A_S + iB_S$), is:

$$R(\mathbf{Q}) = \frac{A_N^2 + B_N^2 + 2PA + q^2B + (A_{PN} - B_S)^2 + (B_{PN} + A_S)^2 + C_+}{A_N^2 + B_N^2 - 2PeA + q^2B + (A_{PN} - B_S)^2 + (B_{PN} + A_S)^2 + C_-} \quad (2.34)$$

in which:

$$A = A_N(q^2 A_M + A_{PN} - B_S) + B_N(q^2 B_M + B_{PN} - A_S) \quad (2.35)$$

$$B = A_M^2 + B_M^2 + 2((A_{PN} - B_S)A_M + (B_{PN} - A_S)B_M) \quad (2.36)$$

and C_{\pm} is the $(\lambda/2)$ correction.

3 SPIN DENSITY RECONSTRUCTION

From the knowledge of the experimental magnetic structure factors (or of the flipping ratios in a non centric case), the spin density can be reconstructed, either without introducing any model, or by refining the parameters of a model in order to fit the experimental data.

3.1 Spin density reconstruction without any model

There are two possible methods to retrieve the spin density from the experimental data (F_M 's in the centric case or R 's in the non centric case) without making any assumption on the cell content: the inverse Fourier summation, which can be applied only if the F_M are determined (i.e. in the centric case), and the Maximum of Entropy method.

Fourier summation

The spin density can be written as an infinite Fourier summation of the experimental magnetic structure factors:

$$\rho_S(\mathbf{r}) = \frac{1}{V} \sum_{\mathbf{Q}} F_M^S(\mathbf{Q}) e^{-i\mathbf{Q}\cdot\mathbf{r}} \quad (3.1)$$

where V is the cell volume.

In practice this summation is limited by the maximal experimental value of $\sin \theta/\lambda$. Moreover only Bragg reflections with a strong enough F_N can be measured and some important magnetic contributions F_M corresponding to weak nuclear reflections may therefore be missing in the Fourier summation leading to artefacts in the spin density reconstruction.

Maximum of Entropy

The first application of the Maximum of Entropy Method (MaxEnt) to spin density determination was performed by R. Papoular [12].

The magnetisation density distribution $\rho(\mathbf{r})$ reconstructed by MaxEnt is the distribution which maximizes the entropy and fills the $\chi^2 = 1$ condition. In order to calculate the entropy, the crystallographic cell is divided according to a grid of $2M$ pixels in which the density is assumed to be constant $\rho(\mathbf{r}) = \rho_i$. However, because the spin density may be as well as negative as positive and because the entropy is defined for positive quantities only, one considers a double distribution of positive quantities $n_i = \rho^+(\mathbf{r}_i)$ and $n_{i+M} = \rho^-(\mathbf{r}_i)$, the magnetisation density being given by $\rho_i = \rho^+(\mathbf{r}_i) - \rho^-(\mathbf{r}_i)$. The entropy of the magnetisation density is then defined by:

$$S(\rho) = - \sum_{i=1}^{2M} p_i \text{Log}(p_i) \quad (3.2)$$

where p_i is the normalised density in pixel i :

$$p_i = \frac{\rho_i}{\sum_{j=1}^{2M} \rho_j} \quad (3.3)$$

and the expression of χ^2 for a set of N unique experimental magnetic structure factors is:

$$\chi^2(\rho) = \frac{1}{N} \sum_{\mathbf{Q}} \frac{|F_M^{\text{exp}}(\mathbf{Q}) - F_M^{\text{calc},\rho}(\mathbf{Q})|^2}{\sigma^2(\mathbf{Q})} \quad (3.4)$$

where $F_M^{\text{calc},\rho}(\mathbf{Q})$ is the magnetic structure factor calculated from the discrete distribution defined above. The MaxEnt method was later adapted to the non centric case [13].

3.2 Model refinement

Two different procedures can be carried out depending on which quantity is modelled: either the unpaired electron wave function or the spin density [14]. In both cases, the model consists in an analytical expression, the parameters of which are refined by fitting the theoretical magnetic structure factors (or flipping ratios in the non centric case) on the experimental data. These parameters are then used to reconstruct the spin density from the analytical model.

Wave function model

In the Restricted Hartree-Fock description of the wave function of a molecular system with one unpaired electron, the spin density is given by the square of the modulus of the singly occupied molecular orbital $\phi(\mathbf{r})$:

$$\rho(\mathbf{r}) = |\phi(\mathbf{r})|^2 \quad (3.5)$$

where the molecular orbital ϕ can be written as a linear combination of atomic orbitals $\psi_i(\mathbf{r}_i)$ centred on atom i :

$$\phi(\mathbf{r}) = \sum_i^{\text{atoms}} \alpha_i \psi_i(\mathbf{r}) \quad (3.6)$$

The atomic orbitals are linear combinations of Slater-type atomic functions:

$$\psi_i(\mathbf{r}_i) = \sum_{L=0}^{N-1} R_L^i(\xi_L^i, r_i) \sum_{M=-L}^L a_{LM}^i Y_{LM}^i(\theta_i, \varphi_i) \quad (3.7)$$

where N , L and M are the atomic quantum numbers: N is the first quantum number ($N = 0$ for $1s$, $N = 1$ for $2s, 2p$; $N = 2$ for $3s, 3p, 3d$); $L = 0$ to $N - 1$, the second quantum number ($L = 0$ for s orbitals; $L = 1$ for p orbitals and $L = 2$ for d orbitals) and M is the magnetic quantum number $M = -L$ to L . $Y_{LM}^i(\theta_i, \varphi_i)$ is a usual spherical harmonics and the radial wave function is a Slater function:

$$R_L^i(\xi_L^i, r_i) = N_r r_i^N e^{-\xi_L^i r_i} \quad (3.8)$$

The coefficients a_{LM}^i are the atomic orbital coefficients with the normalisation condition:

$$\sum_{M=-L}^L (a_{LM}^i)^2 = 1 \quad (3.9)$$

From expression (2.4), the magnetic structure factors can be written as:

$$F_M(\mathbf{Q}) = \int \phi(\mathbf{r})^* e^{i\mathbf{Q}\cdot\mathbf{r}} \phi(\mathbf{r}) d\mathbf{r} \quad (3.10)$$

Using the description of the molecular orbital $\phi(\mathbf{r})$ in (3.6) as a linear combination of atomic orbitals $\psi_i(\mathbf{r})$ leads to terms involving atomic orbitals centred either on the same atom (one-centre) or on two different atoms (two-centre). If the overlap between neighbouring atoms is neglected, the expression of F_M becomes:

$$F_M(\mathbf{Q}) = \sum_i^{atoms} p_i f_m^i(\mathbf{Q}) e^{i\mathbf{Q}\cdot\mathbf{R}_i} e^{-W_i} \quad (3.11)$$

where $f_m^i(\mathbf{Q})$ is the normalised magnetic form factor of atom i , in position \mathbf{R}_i , which carries a spin population p_i :

$$f_m^i(\mathbf{Q}) = \int \psi_i(\mathbf{r})^* e^{i\mathbf{Q}\cdot\mathbf{r}} \psi_i(\mathbf{r}) d\mathbf{r} \quad (3.12)$$

After development of $f_m^i(\mathbf{Q})$ using expression (3.7) of the atomic orbital $\psi_i(\mathbf{r})$, the following expression of F_M is obtained:

$$F_M(\mathbf{Q}) = \sum_i^{atoms} p_i \sum_{L=0}^{\infty} \langle j_L(\mathbf{Q}) \rangle \sum_{M=-L}^L c_{LM} Y_{LM}^*(\theta_Q, \varphi_Q) e^{i\mathbf{Q}\cdot\mathbf{R}_i} e^{-W_i} \quad (3.13)$$

where c_{LM} are related to the products of orbital coefficients $a_{L_1 M_1}^i a_{L_2 M_2}^i$ via the 3j coefficients used to calculate the integral of three spherical harmonics products [7]:

$$c_{LM}^i = i^L (4\pi)^{1/2} (2L+1)^{1/2} (2L_1+1) \begin{pmatrix} L_1 & L_1 & L \\ 0 & 0 & 0 \end{pmatrix} \quad (3.14)$$

$$\times \sum_{M_1, M_2} (-1)^M \begin{pmatrix} L_1 & L_1 & L \\ -M_1 & M_2 & M \end{pmatrix} a_{L_1 M_1}^{i*} a_{L_2 M_2}^i \quad (3.15)$$

and $\langle j_L(\mathbf{Q}) \rangle$ is the Fourier-Bessel transform of the atomic orbital radial function $R_L^{WF}(r)$:

$$\langle j_L(\mathbf{Q}) \rangle = \int_0^{\infty} r^2 (R_L^{WF}(r))^2 j_L(Qr) dr \quad (3.16)$$

$j_L(Qr)$ being the spherical Bessel function.

In the final expression (3.13) of the magnetic structure factor, the parameters to be refined are the atomic spin population p_i and the orbital coefficients a_{LM}^i . A least-squares program was written for $2p$ orbitals by E. Ressouche.

Multipole model

The multipole model applied to spin density (Molly program) [15] was derived from the Hansen & Coppens formalism established for charge density distributions [16]. The spin density is expressed as a sum of atomic densities:

$$\rho(\mathbf{r}) = \sum_i \rho_i^{\text{mult}}(\mathbf{r}_i) \quad (3.17)$$

where $\mathbf{r}_i = \mathbf{r} - \mathbf{R}_i$.

The atomic spin density is developed on the basis of multipole functions:

$$\rho_i^{\text{mult}}(\mathbf{r}_i) = P_v^i R_0^i(\kappa' r_i) + \sum_{l=0}^{l_{\text{max}}=4} R_l^i(\kappa'' r_i) \sum_{m=-l}^l P_{lm}^i y_{lm}^i(\theta, \varphi) \quad (3.18)$$

where the radial function $R_l^i(\kappa r)$ is a Slater-type function of variable κr (κ being a contraction coefficient which can be refined)

$$R_l^i(\kappa r) = \frac{\kappa^3 \zeta_l^{n_l+3}}{(n_l + 2)!} r_i^{n_l} e^{-\kappa \zeta_l^i r_i} \quad (3.19)$$

and $y_{lm}^i(\theta_i, \varphi_i)$ is a real spherical harmonics:

$$y_{lm+} = \frac{1}{2}(Y_{lm+} + Y_{lm-}) \quad (3.20)$$

$$y_{lm-} = \frac{1}{2i}(Y_{lm+} - Y_{lm-}) \quad (3.21)$$

Most of the time, the second term alone is used. The first spherical term in (3.18) permits to refine the atomic density as a sum of two contributions resulting from 2 different types of orbitals ($2s$ and $2p$ in the case of hybridisation for example).

The expression of the magnetic structure factors F_M obtained by Fourier transform of the multipole development (3.17) is very similar to that developed for the wave function model, except that the usual spherical harmonics is replaced by a real spherical harmonics.

$$F_M(\mathbf{Q}) = \sum_i^{\text{atoms}} \sum_{l=0}^4 i^l \langle j_l(\mathbf{Q}) \rangle \sum_{m=-l}^l P_{lm} y_{lm}(\theta_Q, \varphi_Q) e^{i\mathbf{Q}\cdot\mathbf{R}_i} e^{-W_i} \quad (3.22)$$

where $\langle j_l(\mathbf{Q}) \rangle$ are Fourier-Bessel transform of the density radial Slater function $R_l^{\text{dens}}(r)$ (corresponding to the square of $R_L^{WF}(r)$ in (3.8)):

$$\langle j_l(\mathbf{Q}) \rangle = \int_0^\infty r^2 (R_l^{\text{dens}}(r)) j_l(Qr) dr \quad (3.23)$$

In the expression (3.22) of the magnetic structure factor, the parameters to be refined are the multipole coefficients P_{lm}^i and the radial contraction coefficients κ . The initial values of the Slater exponents are deduced from the wave function calculations reported in literature [17], taking $\zeta^i = 2\xi^i$ as the spin density corresponds to a square of atomic orbital.

A least-squares procedure is applied in order to fit the calculated magnetic structure factors to the experimental ones. In the non centric case, flipping ratios are calculated from (2.34) using the expression (3.22) of $F_M(\mathbf{Q})$, which is a complex quantity in that case, all other quantities being introduced

as data. The least-squares refinement is then performed by comparison between the calculated and the experimental flipping ratios. The spin density is reconstructed from expression (3.18) using the refined parameters, P_{lm}^i and κ .

General model

It is possible to reconstruct the spin density using the wave function model for chosen atoms and the multipole model for the other atoms because of the analogy of the two descriptions. It should be noticed that, in this case, $\phi(\mathbf{r})$ in expression (3.5) is not a molecular orbital of the system because it is limited to a certain number of atoms. Moreover it is assumed that this model can be applied to systems with n unpaired electrons ($n > 1$), although $\phi(\mathbf{r})$ should be replaced in (3.5) by a Slater determinant or a linear combination of Slater determinants built on the n unpaired electron molecular orbitals.

The expression of the spin density is developed by replacing $\phi(\mathbf{r})$ by its development over the atomic orbital basis [18]:

$$\rho(\mathbf{r}) = \left| \sum_i^{atoms} \alpha_i \psi_i(\mathbf{r}_i) \right|^2 \quad (3.24)$$

If the interatomic cross terms are neglected, this expression becomes:

$$\rho(\mathbf{r}) = \sum_i^{atoms} \alpha_i^2 |\psi_i(\mathbf{r})|^2 \quad (3.25)$$

In order to allow negative spin populations, the coefficient α_i^2 is replaced by an atomic population parameter p_i that can be positive or negative. This corresponds to the atomic orbital model:

$$\rho_i^{at}(\mathbf{r}_i) = p_i |\psi_i(\mathbf{r}_i)|^2 \quad (3.26)$$

The atomic orbital has a similar expression to (3.7) where the spherical harmonics is replaced by a real spherical harmonics:

$$\psi_i(\mathbf{r}_i) = R_{N,L}^i(\xi_L^i, r_i) \sum_{M=-L}^L a_{LM}^i N_{ang} y_{LM}^i(\theta_i, \varphi_i) \quad (3.27)$$

where the radial wavefunction is a Slater function and a_{LM}^i are the atomic orbital coefficients with the normalisation condition (3.9).

The expression of the atomic spin density in (3.26) is developed with help of the following properties:

- the product of Slater-type functions is a Slater-type function

$$R_{N,L}^i(\xi_L^i, r_i) R_{N,L}^i(\xi_L^i, r_i) = \aleph^2 r_i^{2N} e^{-2\xi_L^i r_i} \quad (3.28)$$

- the product of spherical harmonics is a linear combination of spherical harmonics

$$y_{LM_1}^i(\theta, \varphi) y_{LM_2}^i(\theta, \varphi) = \sum_{l=1}^{l_{max}} c_l y_{l, M_1+M_2}^i(\theta, \varphi) \quad (3.29)$$

The final expression of the atomic spin density takes the form:

$$\rho_i^{at}(\mathbf{r}_i) = R_{2N,L}^i(2\xi_L^i, r_i) \sum_{l=1}^{l_{max}} \sum_{m=-l}^l P_{l,m}^i y_{l,m}^i(\theta, \varphi) \quad (3.30)$$

where the coefficient P_{lm}^i is a linear combination of products of atomic coefficients.

The expression (3.30) is similar to the second term of the multipolar development (3.18) at the condition that a same radial function is taken for all multipoles $l = 1$ to l_{max} , with exponents $n_l = 2N$ and $\zeta_l^i = 2\xi_L^i$. The relationships between the atomic orbital coefficients a_{LM}^i and the multipole coefficients P_{lm}^i were established for $2p$ [11] and extended to $3d$ orbitals [7]. They were introduced as constraints in the multipole refinement program in a modified version of the Molly program, which permits to refine the orbital coefficients for chosen atoms i and obtain the corresponding multipole populations (MOL3D program [7]). The CCSL library also permits to perform multipole refinements using form factors calculated either from a radial wave function or from multipole radial functions [19].

At the same time, multipole coefficients can be refined for the other atoms i' :

$$\rho(\mathbf{r}) = \sum_i \rho_i^{at}(\mathbf{r}_i) + \sum_{i'} \rho_{i'}^{mult}(\mathbf{r}_{i'}) \quad (3.31)$$

The spin density in the molecule is then reconstructed from the multipole parameters for all atoms.

4 MOLECULE-BASED MAGNETISM

Molecule-based magnetic materials are solid compounds built from molecular fragments like organic radicals and transition metal (or rare earth) ions complexes. Two main effects are characteristic of this type of materials: the spin delocalisation and spin polarisation effects over the molecule due to the strong magnetic moment localised on one atom. The first effect is responsible for a contribution on neighbouring atoms of same sign as the magnetic atom and spin polarisation gives an opposite sign contribution.

The magnetic interaction between two magnetic atoms, for instance transition ions coupled by an organic bridge, can be described by the magnetic coupling between two molecular entities A and B coupled by magnetic superexchange or by charge transfer in the AB system [1]. The active electron approximation consists in considering only the unpaired electrons occupying magnetic orbitals built on d orbitals of the metallic ion and orbitals of the neighbouring ligands.

4.1 Magnetic superexchange

The exchange hamiltonian between local spins S_A and S_B is written [20]:

$$H = -J S_A S_B \quad (4.1)$$

where J is the magnetic coupling constant. In the case where each entity A and B carries only one unpaired electron in a and b orbitals respectively, J can be written as the sum of two terms:

$$J = K + 2\beta S \quad (4.2)$$

where K is the two-electron exchange integral involving the two singly occupied magnetic orbitals a and b :

$$K = \langle a(1) b(2) | \frac{e^2}{r_{12}} | a(2) b(1) \rangle \quad (4.3)$$

and β is

$$\beta = \langle a|h|b \rangle \quad (4.4)$$

h is the mono-electronic hamiltonian taking into account the kinetic energy of the active electron and its interaction with the nuclei and the passive electrons. S is the overlap integral between the magnetic orbitals:

$$S = \langle a|b \rangle \quad (4.5)$$

The first term K is always positive and therefore favours a ferromagnetic interaction. At the opposite, the $S\beta$ product is always negative (if S is non zero) and favours an antiferromagnetic interaction. The coupling constant may be then written as the sum of two ferro and antiferromagnetic contributions:

$$J = J_F + J_{AF} \quad (4.6)$$

The AF term is proportional to the overlap integral S and is favoured by a large overlap between the magnetic orbitals, which is the most usual case in nature.

The main mechanisms leading to a ferromagnetic interaction are:

- the strict orthogonality between the magnetic orbitals for symmetry reasons,
- the accidental orthogonality (spin delocalisation mechanism) due to geometrical conditions,
- the spin polarisation (or 1st Mc Connell) mechanism, which occurs when there is an overlap between a region of strong positive spin density and a region of weak negative density due to intramolecular spin polarisation.

4.2 Charge transfer

Charge transfer concerns compounds (AB) formed by two molecular fragments A and B , in which one electron is transferred from A to B , or from B to A , to form an excited charge transfer state, (A^+B^-) or (A^-B^+). Ferromagnetic coupling may be favoured when the charge transfer occurs from a singly occupied orbital of A (or B), a_1 (or b_1), towards an empty orbital of B (or A), b_2 (or a_2), or when each unpaired electron occupies degenerate orbitals (a_1, a_2) on the A side and (b_1, b_2) on the B side. The coupling between the AB triplet state (a_1b_1) with the lowest energy charge transfer triplet state (a_1a_2) or (b_1b_2) stabilizes in this case the triplet ground state.

5 SPIN DISTRIBUTIONS IN ORGANIC RADICALS

This section is devoted to compounds in which magnetism originates from $2p$ unpaired electrons carried by organic groups, so-called organic radicals. PND provides a direct test of the magnetic interaction pathways as it gives evidence for the atoms carrying some spin density, which are therefore involved in magnetic interactions [21]. The first example is a paramagnetic biradical $\text{Ti}(\text{L})_2$ formed by two semiquinonate radicals, coordinated to a non-magnetic Ti^{4+} ion, which are ferromagnetically coupled. The second compound Nit-py, purely organic, forms ferromagnetic chains of nitronyl nitroxide radicals connected by through H bonds.

5.1 Intramolecular Ferromagnetic superexchange between semiquinonate radicals via a non magnetic Ti^{4+} ion in the biradical $\text{Ti}^{\text{IV}}(\text{Cat-N-SQ})_2$

The biradical $\text{Ti}^{\text{IV}}(\text{Cat-N-SQ})_2$ is a typical example of intramolecular ferromagnetic coupling resulting from the orthogonality between the magnetic orbitals of the two Cat-N-SQ radicals coordinated to the central non magnetic Ti^{4+} ion ($3d^0$). The radical Cat-N-SQ is planar and has the formula schematised in Figure 3. The unpaired electron is delocalised over the molecular fragment in a π orbital.

The Ti^{4+} ion lies in an octahedral environment, formed by the two nitrogen atoms in axial position and the four oxygen atoms in equatorial position, the radical planes being orthogonal to each other. Each radical is coordinated to Titanium through two O-Ti bonds and one N-Ti bond. The magnetic behaviour of this compound is that of a triplet ($S = 1$) paramagnetic ground state reflecting the ferromagnetic coupling between the two local spin 1/2 associated to each radical. The ferromagnetic nature of the coupling was clearly assigned to the orthogonality of the radical planes but an uncertainty between two possible interaction pathways was remaining: - either there is a direct contact between the magnetic orbitals at the oxygen positions which lies at distances of 2.7\AA from each other or the interaction is indirect via the Ti^{4+} ion due a spin transfer from the ligands towards the Ti^{4+} diffuse orbitals.

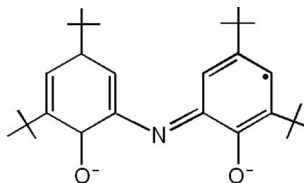


Figure 3. The Cat-N-SQ radical.

The determination of the spin density map permitted to discriminate between these two exchange pathways [22]. Polarised neutron measurements were performed on the diffractometer 5C1 (LLB-Orphée) at 1.5 K under an applied field of 7 Tesla providing a set of 39 magnetic structure factors. A multipole model (see section 3.2.2) limited to spherical terms was refined. The radial coefficients taken from literature [17] are reported in Table 1. A goodness of fit of 1.31 and an agreement factor R_W of 0.16 were obtained. The experimental spin populations given by the monopole populations are compared in Table 1 to the Mulliken atomic spin populations calculated by the DFT method.

Table 1. Refined spin populations (in μ_B) and DFT calculated spin populations.

atom	neutron study			DFT calculations	
	radial coefficients		monopole populations (in μ_B)	atomic spin populations	
	n_l	ζ (a.u. ⁻¹)	P_{00}	p_i	
C	2	3.44	0.22(5)	2p	0.11
N	2	3.9	0.20(7)	2p	0.26
O	2	4.5	0.02(6)	2p	0.06
Ti	4	5.4	0.17(3)	3d, 3p	0.08

The spin density map is represented in Figure 4 in projection along the bisecting direction of the $\widehat{O_1TiO_2}$ angle.

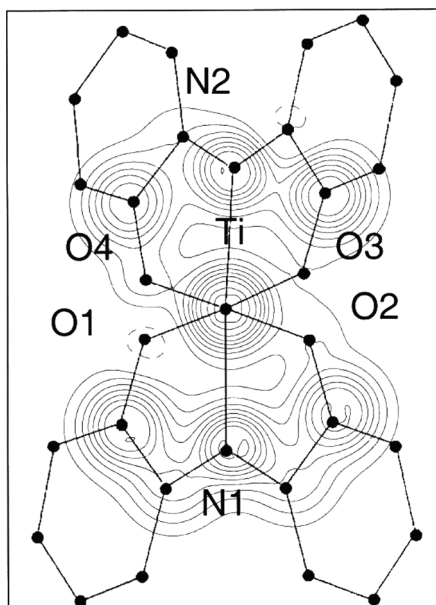


Figure 4. Spin density map in $Ti^{4+}(Cat-N-SQ)_2$ in projection along the bisecting direction of the $\widehat{O_1TiO_2}$ angle. Step: $0.02 \mu_B \cdot \text{\AA}^{-2}$ (positive contours are continuous lines and negative contours are dashed).

The spin density is mainly delocalised on the nitrogen atoms and on the carbon atoms belonging to the four CO bonds of the radicals, but no significant spin density lies on the oxygen atoms. A positive magnetic moment of $0.17(3)\mu_B$ is found on the titanium atom, which indicates that a spin transfer occurs from the radical towards the $3p$ or $3d$ diffuse orbitals of the Ti^{4+} ion. This demonstrates that the ferromagnetic interaction is due to indirect superexchange via the Ti^{4+} orbitals. DFT calculations are in qualitative agreement with these results but underestimate the spin delocalisation towards the titanium and carbon atoms.

5.2 Intermolecular ferromagnetic superexchange between nitronyl nitroxide Nit-Py radicals through H bonding

Extended structures can be obtained owing to the ability of nitronyl nitroxide organic radicals to build long range ordered systems. The nitronyl nitroxide radical (Nit) is represented in Figure 5. The unpaired electron is delocalised mainly over the two NO bonds, with equal distribution on the four atoms, and can be described by a π molecular orbital.

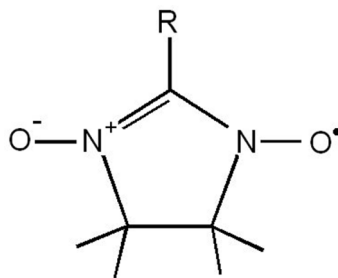


Figure 5. The nitronyl nitroxide radical.

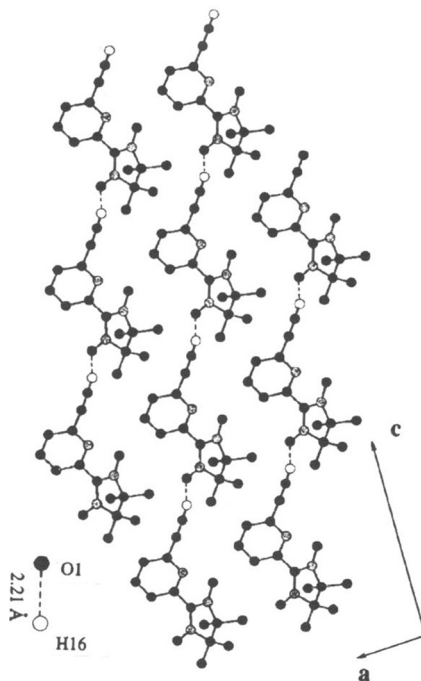


Figure 6. Crystallographic structure of the radical Nit-py in projection along the **b** axis.

The first purely organic radical which was found to exhibit ferromagnetic ordering at low temperature ($T_C = 0.67$ K) is a nitronyl nitroxide radical Nit-R where R = para-nitrophenyl is the substituting group. This compound was investigated by polarised neutron diffraction [23], which permitted to give evidence for the roles of the accidental orthogonality and spin polarisation mechanisms in the two types of ferromagnetic intermolecular exchange interactions. The compound Nit-py, where py = 2-(6-ethynyl-2-pyridyl), which is described here, forms chains of radicals which are related to each other by an hydrogen bond [24].

A weak intrachain ferromagnetic coupling $J = 0.9$ K (1.4 cm^{-1}) was observed. The compound displays AF ordering between the chains at 0.61 K. A data collection was performed at 4.75 K under 8 Tesla on the polarised neutron diffractometer DN2 installed at the Siloe reactor of the CENG in Grenoble (DN2 was later moved to the ILL and became D23 after renewing). The maximum of entropy method on the set of 196 F_M 's gave evidence of a positive density on the hydrogen atom H_{16} that is involved in the $N_2-O_1 \cdots H_{16}$ hydrogen bond [25].

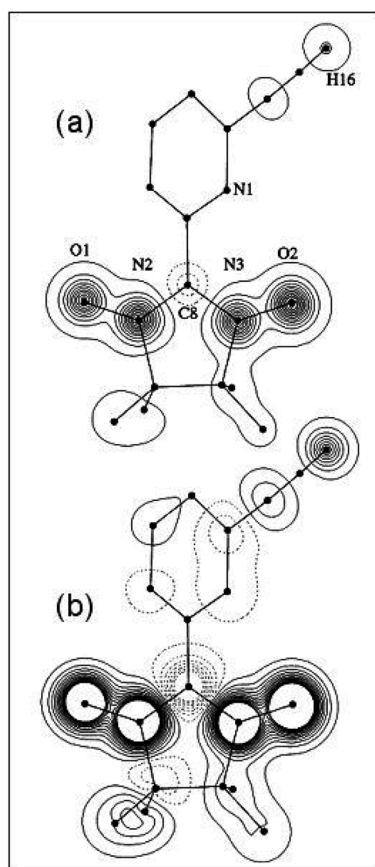


Figure 7. Reconstructed spin density in Nit-py in projection onto the nitroxide mean plane: (a) high-level contours (step: $0.04 \mu_B \cdot \text{\AA}^{-2}$); (b) low-level contours (step: $0.008 \mu_B \cdot \text{\AA}^{-2}$).

The induced spin density map was reconstructed from a model in which $2p_z$ -type orbitals were assumed for the four atoms of the two NO groups and the central carbon C_8 , the z axis being perpendicular to the Nit plane. All other atoms, including the H_{16} atom, were refined in a spherical model (see section 3.2.3). The radial orbital exponents were for O, N, C: $n_l = 2$, $\xi = 2.25, 1.95$ and 1.72 (a.u. $^{-1}$) and for H, $n_l = 0$ and $\xi = 2.50$ (a.u. $^{-1}$). Radial contraction coefficient were refined for N and O: $\kappa_N = 1.02(2)$ and

$\kappa_O = 0.90(1)$. The final GOF is equal to 1.22. The reconstructed spin density represented in Figure 7, in projection onto the Nit plane, illustrates the spin delocalisation over the molecule.

A visualisation of the $2p_z$ -type densities on the ONCNO group is provided in Figure 8 by the projection of the spin density along the perpendicular to the NN direction in the Nit plane.

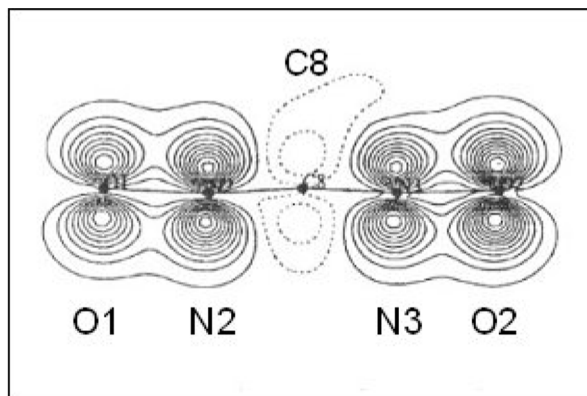


Figure 8. Reconstructed spin density in Nit-py in projection onto the nitroxide π plane. Step: $0.04 \mu_B \cdot \text{\AA}^{-2}$ (negative contours are dashed).

Two important features have to be noticed: first of all, a significant positive spin population, $P_{H_{16}} = 0.04(1)\mu_B$, is observed on H_{16} ; secondly, the spin population of the O_1 oxygen atom involved in H bonding ($P_{O_1} = 0.20(1)\mu_B$) is clearly lower than the population of the O_2 atom ($P_{O_2} = 0.28(1)\mu_B$) of the other NO group, while the nitrogen atoms carry equivalent populations ($P_{N_2} = 0.24(1)$ and $P_{N_3} = 0.22(1)\mu_B$) in both NO groups. This suggests that an electron transfer from O_1 towards H_{16} is mediated by H bonding. These results are in favour of the interpretation of ferromagnetic coupling between neighbouring radicals along the chain by a charge transfer mechanism. DFT calculations show that this charge transfer can occur between the single occupied π^* orbital of the nitronyl nitroxide group towards the lowest unoccupied magnetic orbital of the neighbouring radical which has a contribution on H_{16} .

6 SPIN DISTRIBUTIONS IN COMPOUNDS INCLUDING TRANSITION METAL IONS

The most usual molecule-based magnetic materials are built from organic complexes of magnetic transition metals ions. The organic ligands may be radicals [14], carrying themselves unpaired electrons, or organic bridges which mediate the magnetic interaction between transition metal ions [26]. The two kinds of compounds are described in this section: a copper-nitroxide compound forming ferromagnetic chains of spin 1/2, and a bicopper paramagnetic complex presenting a large intramolecular ferromagnetic coupling via two azido bridges N_3^- . The advantages of the flipping ratio technique for studying magnetic interactions, which are emphasized below, are the visualization of the orientation of the magnetic orbitals and the determination of the sign of the atomic spin densities. Another type of application of PND to molecule-based magnetism concerns high spin clusters. The determination of the spin distribution in a paramagnetic cluster allows elucidating without any ambiguity the nature of the spin ground state, while magnetic measurements do not always give a unique solution for the spin arrangement.

6.1 Ferromagnetic chains -Cu-Nit-Cu-

The compound $\text{Cu}(\text{hfac})_2\text{NitMe}$ forms ferromagnetic chains of spin 1/2 with alternating Cu^{2+} ions and Nit radicals, $-\text{Cu}_1-\text{Nit}-\text{Cu}_2-\text{Nit}-$, with two copper sites in different surroundings [27] (Figure 9). Each of

the two NO groups of one Nit radical lies in axial coordination of the neighbouring octahedral copper, the Nit plane being nearly parallel to the basal plane of the copper.

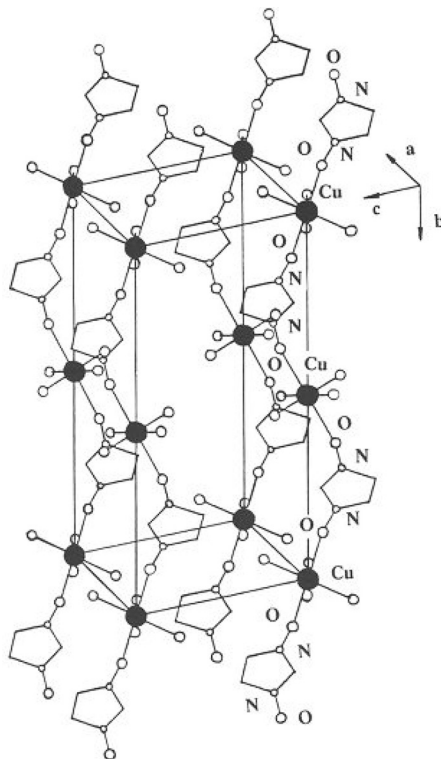


Figure 9. Cell content for the $\text{Cu}(\text{hfac})_2\text{NitMe}$ compound.

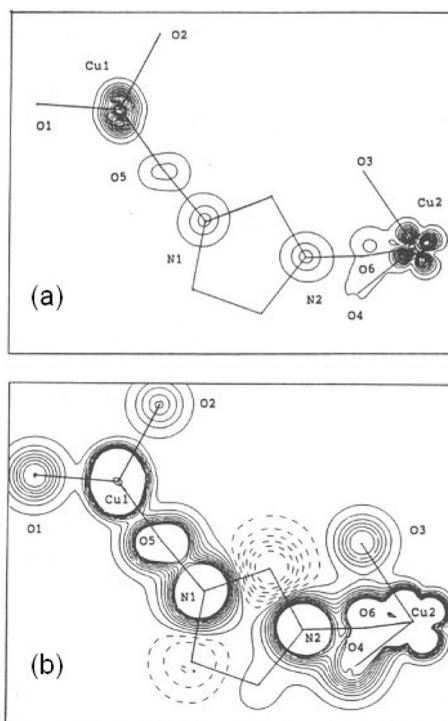
A wave function model, as described in section 3.2.1, was used to refine the spin density on 162 unique magnetic structure factors measured on D3 (ILL) at 2.5 K with an applied field of 4.6 Tesla. The initial radial orbital exponents ξ (a.u.⁻¹) were the same as those given in paragraph 5.2 for N, O, C and a value of 4.40 a.u.⁻¹ was taken for Cu from literature [17]. The local axes were defined with respect to the bond directions: $z_{\text{Cu}} // \text{Cu-ON}$, $y_{\text{Cu}} // \text{Cu-O (hfac)}$ and $x_{\text{Cu}} \perp (y, z)$ for each copper atom and $z_{\text{NO}} \perp \text{Nit plane}$, $y_{\text{NO}} // \text{NO}$, $x_{\text{NO}} \perp (y, z)$ for each NO group.

The coefficients of the 3d copper orbital and 2s, 2p orbitals centred on N and O were refined, as well as the corresponding atomic spin populations. For the oxygen atoms belonging to the hfac ligand and the carbon atoms of the Nit ring, spherical contributions to the molecular orbital were refined. The contraction coefficients remain very close to unity after refinement: $\kappa_{\text{Cu}} = 1.06(3)$, $\kappa_{\text{N}} = 1.00(3)$, $\kappa_{\text{O}} = 1.06(5)$. In Table 2 are reported the orbital coefficients and spin populations for the Cu, N and O atoms of the Nit radical obtained in the final refinement (GOF = 2.55) and the corresponding experimental spin density map, in projection onto the Nit plane, is shown in Figure 10.

The sum of the populations over each -Cu-Nit- unit, which amounts 1.89(3) μ_B , is in agreement with the magnetisation value in the same conditions of temperature and field (1.91 μ_B). The total moment carried by the radical, 0.88 μ_B , is of the same order of magnitude than on each copper fragment (Cu and the four (hfac) oxygen atoms) which shows that the spins 1/2 are uniformly distributed on the Cu and Nit sites in the chain. In the radical, it is to notice that the nitrogen atom carries a larger spin population than the oxygen atom of each NO bond, in contrast with free nitroxide radicals where the spin density is almost equally distributed on N and O [28]. A spin transfer from oxygen towards nitrogen occurs together with the formation of the chains.

Table 2. Refined atomic spin populations (in μ_B) and orbital coefficients for the Cu atoms and NO groups in Cu(hfac)₂NitMe.

		copper atoms		nitronyl nitroxide radical					
		Cu ₁	Cu ₂		N ₁	N ₂	O ₅	O ₆	
atomic	$3d_{x^2-y^2}$	-0.60(17)	0.91(11)	$2s$	0.18(3)	-0.04(3)	-0.15(5)	-0.28(6)	
orbital	$3d_{z^2}$	-0.33(13)	0.03(16)	$2p_x$	-0.40(7)	-0.11(12)	-0.56(13)	0.77(6)	
coefficients	$3d_{xy}$	0.42(8)	0.34(19)	$2p_y$	-0.12(9)	-0.18(8)	0.29(15)	-0.02(12)	
	$3d_{xz}$	0.05(11)	0.24(20)	$2p_z$	0.89(3)	0.98(2)	0.77(6)	0.57(7)	
	$3d_{yz}$	0.59(17)	0.00(15)						
atomic spin	$3d$	0.858(9)	0.754(8)	$2s$	0.010(3)	0.001(1)	0.004(3)	0.015(7)	
population				$2p$	0.311(8)	0.299(8)	0.205(7)	0.190(10)	

**Figure 10.** Reconstructed spin density in Cu(hfac)₂NitMe in projection onto the Nit plane: (a) high levels of isodensity: step $0.2 \mu_B \cdot \text{\AA}^{-2}$; (b) low levels: step $0.005 \mu_B \cdot \text{\AA}^{-2}$.

The copper Cu₂ orbital is predominantly of $3d_{x^2-y^2}$ type and the Cu₁ orbital appears to be more distorted (combination of $3d_{z^2}$, $3d_{xy}$, $3d_{yz}$ and $3d_{x^2-y^2}$). The N₁ and N₂ orbitals are mainly of $2p_z$ type, while the O₅ and O₆ oxygen $2p$ orbitals have predominant coefficients on both $2p_x$ and $2p_z$. This corresponds to a tilt of the $2p$ oxygen orbital towards the x direction, perpendicular to the NO bond, which lies in the Nit plane and is nearly in the neighbouring copper basal plane. It can be seen on the density map in Figure 10 that the orientation of the oxygen O₆ orbital is almost parallel to the Cu₂ basal plane. This is accompanied by a significant $2s$ contribution reflecting some hybridisation of the oxygen atom coordinated to copper. The Figure 11 schematises the orientation between the oxygen $2p$ orbital and the copper $3d$ orbital in each site Cu₁ and Cu₂ deduced from the spin density refinement.

The overlap integral between the copper and oxygen magnetic orbitals is minimized by the relative orientation of the orbitals which make angles of about 20 degrees only between the $2p$ direction and the $3d$ plane. The mechanism of ferromagnetic coupling is therefore consistent with the scheme of accidental orthogonality.

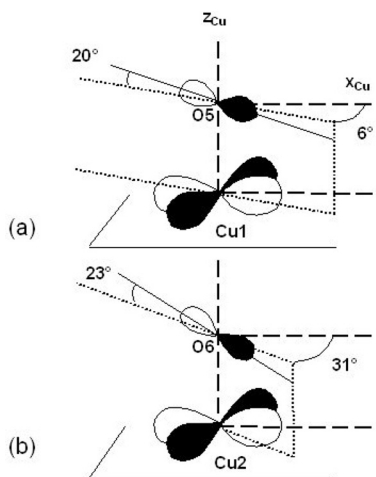


Figure 11. Relative orientation between the copper and oxygen magnetic orbitals for the two sites Cu_1 and Cu_2 .

6.2 Intramolecular Cu-Cu ferromagnetic coupling through ‘end-on’ N_3^- bridging groups

The azido bridge N_3^- occupies a particular place in the large variety of organic bridges used in molecular magnetism. For all the symmetrical di- μ -azido copper(II) dimers synthesized up to now, either a strong ferromagnetic coupling or alternatively a strong antiferromagnetic coupling occurs, depending on the way in which both azido groups are bridging, either in an ‘end-on’ ($\mu - 1, 1-$) or an ‘end-to-end’ ($\mu - 1, 3-$) fashion. Until recently, a long controversy had been developed concerning the origin of the strong ferromagnetic coupling in ‘end-on’ bridged di- μ -azido copper (II) dimers [29]. The two principal mechanisms that were invoked are:

- the spin delocalisation mechanism responsible for the accidental orthogonality of the copper magnetic orbitals delocalised on the bridging nitrogen atoms: the sign of the coupling constant depends on the value of the bridging angle CuNCu [30],

$$J(\text{cm}^{-1}) = -C \alpha(\text{deg.}) + D \quad (6.1)$$

where C and D are empirical values for a series of compounds of the same family.

- the spin polarisation mechanism, which implies the presence of negative spin density on the bridging atoms and predicts a ferromagnetic coupling whatever the bridging angle is.

Because these two mechanisms predict contradictory signs for the spin density on the bridging nitrogen atoms, the experimental spin density determination provides a deciding test for discriminating them. Polarised neutron measurements were performed on D3 at the ILL on the ‘end-on’ bridged molecular compound $\text{Cu}_2(\text{t-bupy})_4(\text{N}_3)_2(\text{ClO}_2)_2$ (with t-bupy = *p-tert*-butylpyridine) which presents a large singlet-triplet gap of 105 cm^{-1} between the triplet paramagnetic ground state ($S = 1$) and the singlet excited state [31]. A set of 152 magnetic structure factors ($F > 3\sigma$) was obtained at 1.6 K under an applied field of 4.6 Tesla, after correction for the copper orbital contribution using the dipolar approximation with $g_{\text{Cu}} = 2.15$. The maximum of entropy method showed that a positive spin density region was located at the bridging nitrogen position. A spin density model refinement was performed using the general model described in section 3.2.3. The n and ζ radial density coefficients were: $n = 4$, $\zeta = 8.8 \text{ a.u.}^{-1}$ for Cu; $n = 2$, $\zeta = 3.9 \text{ a.u.}^{-1}$ for N and $\zeta = 3.44 \text{ a.u.}^{-1}$ for C. A contraction coefficient was refined for Cu and N ($\kappa_{\text{Cu}} = 1.10(1)$ and $\kappa_{\text{N}} = 1.90(1)$). Monopoles populations were refined for the N and C atoms of the pyrimidine rings. Different types of orbital constraints were checked for Cu and for the N atoms of the azido group. The best agreement factors, $R_W(F) = 0.065$ and $\text{GOF} = 1.45$, were

obtained when applying a $3d_{xy}$ or $3d_{x^2-y^2}$ -type constraint on the copper (i.e. in the basal plane) and p_x on the terminal azido nitrogen (x being // Cu...-Cu). The refined atomic spin populations, normalised to $2 \mu_B$, are reported in Table 3.

Table 3. Experimental and theoretical DFT atomic spin populations.

atom	spin populations			
		neutrons	DFT (Mulliken)	
Cu	$3d_{x^2-y^2}$	0.783(7)	$3d$	0.425
N ₁	P_{00}	0.069(6)	$2p$	0.167
N ₂	P_{00}	-0.016(6)	$2p$	-0.005
N ₃	$2p_x$	0.057(7)	$2p$	0.122
N ₄	P_{00}	0.067(8)	$2p$	0.129
N ₅	P_{00}	0.049(7)	$2p$	0.120

The spin is mainly localised on the copper ions but positive spin density on the bridging and terminal nitrogen atoms of the azido bridge is observed as well as on the nitrogen atom of the pyridine rings. The induced spin density map is represented in Figure 12.

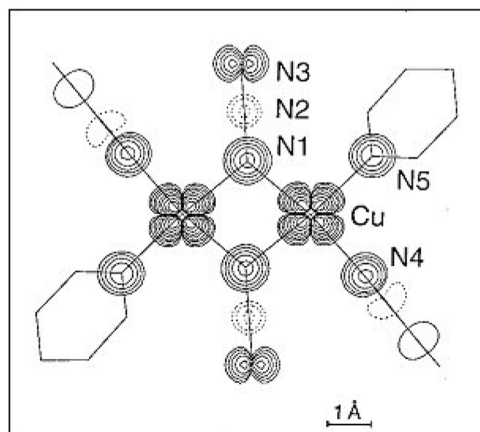


Figure 12. Spin density map in $\text{Cu}_2(\text{t-bupy})_4(\text{N}_3)_2(\text{ClO}_2)_2$ projected onto the central bridge. Logarithmic levels of isodensity: $\pm 0.005 \times 2^{n-1} \mu_B \cdot \text{\AA}^{-2}$.

The positive sign on the bridging nitrogen atom N₁ definitely rules out the spin polarization mechanism and demonstrates that the spin distribution is mainly due to a spin delocalisation mechanism. However, the spin density map also reveals the existence of some negative spin density on the central nitrogen atom N₂, which can be assigned to the spin polarisation of the doubly-occupied azido bridge π_g -type orbital, which is superimposed upon the spin delocalisation mechanism.

The spin populations calculated by the DFT-B3LYP method using the Gaussian 94 program for the triplet ground state are given in Table 3. This method predicts a singlet ground state for an angle α larger than 104 degrees in agreement with the spin delocalisation mechanism. The spin delocalisation is overestimated as always in DFT calculations on copper-containing compounds, but the spin alternation on the azido bridge, due to spin polarisation, is in agreement with the experiment.

6.3 Nature of the ground state in a high spin cluster Fe_8^{III}

The Fe_8Br_8 cluster, $\{[(\text{tacn})_6\text{Fe}_8\text{O}_2(\text{OH})_{12}]\text{Br}_7 \cdot \text{H}_2\text{O}\}[\text{Br} \cdot 8\text{H}_2\text{O}]$, (with tacn = 1, 4, 7-triazacyclononane) has attracted special attention in recent years as displaying pure quantum tunnelling of the

magnetization [3]. Another interesting feature is the strong magnetic anisotropy of the cluster, although each Fe^{III} ion ($S = 5/2$) is individually isotropic. This cluster, formed by eight Fe^{III} ions linked by oxo and hydroxo bridges, has the well-known ‘butterfly’ structure. A model with six spin up and two spin down ions was proposed from the magnetic susceptibility measurements, for the spin configuration of the magnetic ground state $S = 10$, resulting from the competition between various intra-cluster antiferromagnetic interactions.

In order to determine the exact nature of the spin ground state, the magnetisation density was determined by polarised neutron diffraction on D3 at the ILL for the Fe_8Br_8 cluster, which crystallizes in the non centric space group P1 [32]. The induced magnetisation density map at 2 K under a field of 4.6 T displayed in Figure 13 was reconstructed using the MaxEnt method applied to non centric structures [13].

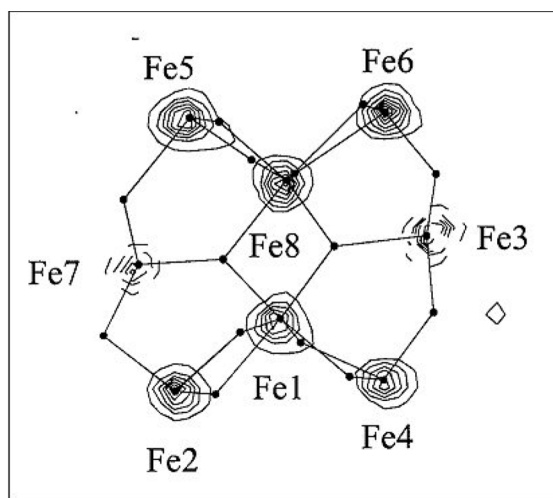


Figure 13. MaxEnt reconstructed spin density in Fe_8Br_8 , in projection onto the (b, c) plane (negative contours are dashed, step $0.7 \mu_B \cdot \text{\AA}^{-2}$).

A model of the spin density was then refined on the basis of 198 experimental flipping ratios. This model consists of a sum of spherical atomic spin densities on the Fe sites, with radial orbital exponents $\zeta_{\text{Fe}} = 7.46 \text{ a.u.}^{-1}$ from [17]. A common radial contraction coefficient κ_{Fe} was refined for the iron atoms: $\kappa_{\text{Fe}} = 0.499(1)$. The map shown in Figure 13 confirms that six ions carry spins parallel to the applied field, which are the body ions 1 and 2 and the four peripheral ions, while the ions 3 and 4 of the wings carry opposite spins, in agreement with the previously proposed model. However, the spin distribution strongly deviates from the D2 symmetry which can be assumed owing to the molecular framework: the spin populations on the body ions Fe_1 [$4.79(22) \mu_B$] and Fe_2 [$2.34(26) \mu_B$] are very different from each other, as well as the populations on the wings Fe_3 [$-1.94(31) \mu_B$] and Fe_4 [$-4.91(32) \mu_B$]. This could reflect the existence of intermolecular magnetic interactions, the corresponding iron atoms being in different environments.

In order to check if this asymmetry is significant or only due to an artefact related to the particular case of a non centric space group, a polarised neutron diffraction experiment was recently performed on 5C1 at the LLB on a centrosymmetric cluster Fe_8pcl [33]. This compound, of formula $[(\text{tacn})_6\text{Fe}_8\text{O}_2(\text{OH})_{12}]\text{Br}_{4.3}(\text{ClO}_4)_{3.7} \cdot 6\text{H}_2\text{O}$, presents essentially the same central core as Fe_8Br_8 , but with a centre of symmetry, and crystallizes in the centrosymmetric space group $\text{P2}_1/\text{c}$ with two cluster molecules in the cell [34]. The magnetic properties of Fe_8pcl are very similar to those of Fe_8Br_8 with a $S = 10$ spin ground state.

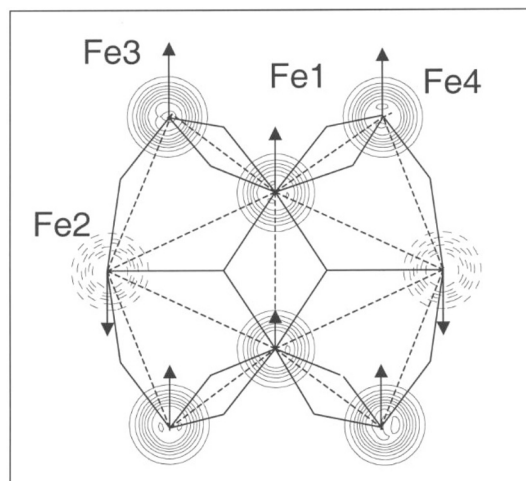


Figure 14. Projection of the induced spin density at 1.8 K under 7 T in Fe_8pcl along the perpendicular to the plane of the butterfly body. Low isodensity levels only: $\pm 0.5 \mu_B \cdot \text{\AA}^{-2}$ with steps of $0.5 \mu_B \cdot \text{\AA}^{-2}$. The structure of the core and the magnetic interaction pathways are schematised on the map.

A spherical spin density model similar to that defined for Fe_8Br_8 was refined on the basis of 52 experimental magnetic structure factors with $F_M > \sigma$ ($T = 1.8 \text{ K}$, $H = 7 \text{ T}$). A weighted agreement factor $R_W(F) = 0.104$ and a goodness of fit $\chi = 2.31$ were obtained. The spin density localized on the iron atoms in Fe_8pcl appears to be less diffuse than in Fe_8Br_8 as shown by the different radial contraction coefficients: $\kappa_{Fe} = 0.89(6)$ in Fe_8pcl with respect to $\kappa_{Fe} = 0.499(1)$ in Fe_8Br_8 . The sum of the refined populations amounts $16.6(4) \mu_B$ that is 87 per cent of the experimental magnetisation value (equal to $19 \mu_B$ at 1.8 K under 7 Tesla). The corresponding spin density map is represented in projection along the perpendicular to the butterfly body in Figure 14.

The relative spin arrangement is in agreement with the previous spin density study in Fe_8Br_8 with positive spin populations on Fe_1 , Fe_3 and Fe_4 and negative ones on Fe_2 . The spin populations of the body ions Fe_1 and Fe_2 in absolute magnitude (around $3\mu_B$) are smaller than the spin populations on the Fe_3 and Fe_4 of the wings (around $4\mu_B$). It is worth to notice that the Fe_1 and Fe_2 spin populations in Fe_8pcl correspond to the mean values of the (Fe_1 , Fe_2) and (Fe_3 , Fe_4) spin populations respectively found in the non centric Fe_8Br_8 . The dissymmetry of the spin density map in the non centric case is therefore more probably due to the data treatment rather than to dissymmetric intermolecular magnetic interactions with different surroundings.

7 APPLICATION TO A PHOTOSWITCHABLE MOLECULAR COMPOUND

Spin crossover compounds containing the Fe^{2+} ion can be switched by varying temperature or pressure, or by light irradiation, from a low spin (LS) diamagnetic state ($S = 0$) to a high spin (HS) paramagnetic state ($S = 2$) and vice versa as schematised in Figure 15.

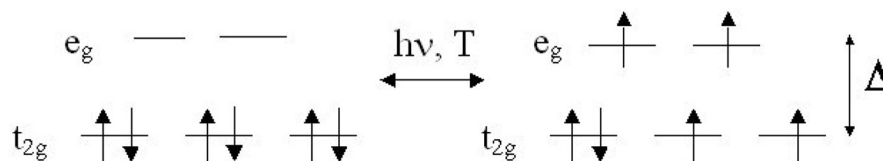


Figure 15. Transition between the $S = 0$ ground state and the $S = 2$ excited state in a $\text{Fe}^{2+} \bar{n}$ complex.

Photo-excitation at low temperature, with light of suitable wavelength, induces a transition of the system in the LS ground state towards a HS meta-stable state having an extremely long lifetime at low temperatures. This effect is therefore called Light Induced Excited Spin State Trapping (LIESST) [35]. Application of PND to study the photo-induced magnetic state of the $[\text{Fe}(\text{ptz})_6](\text{BF}_4)_2$ (ptz = 1-propyltetrazole) spin crossover compound is described in this section.

The photo-switching process was observed by using a new experimental setup allowing both light illumination and polarised neutron diffraction measurements (PND) [36] as schematised in (Figure 16).

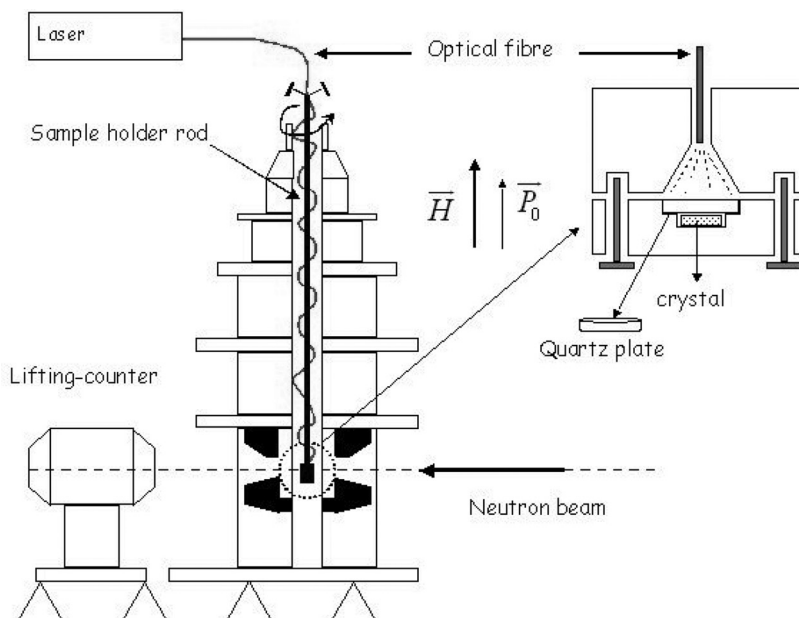


Figure 16. Instrumental setting for in-situ photoexcitation on 5C1.

$[\text{Fe}(\text{ptz})_6](\text{BF}_4)_2$ crystallizes in the trigonal $R\bar{3}$ space group. Upon slow cooling, $[\text{Fe}(\text{ptz})_6](\text{BF}_4)_2$ exhibits a thermal spin transition from the high temperature (HS) phase to the low temperature (LS) phase, with $T_C^\downarrow = 128$ K and $T_C^\uparrow = 135$ K, at ambient pressure, accompanied by a crystallographic phase transition around 130 K from $R\bar{3}$ to P1 at low temperature. Upon fast cooling, the crystallographic phase transition can be suppressed, so that the crystal remains in the $R\bar{3}$ space group even at low temperature. The crystal was therefore first quenched in liquid nitrogen and set in the cryomagnet installed on the 5C1 diffractometer, then cooled down to 2 K. The magnetic field was applied parallel to the c -axis. The crystal was exposed to a laser illumination of $3 \text{ mW}/\text{cm}^2$ at the optical wavelength $\lambda = 473$ nm. The light direction was perpendicular to the crystal surface.

The time dependence of the photo-excitation process of the crystal was followed directly by PND in a constant magnetic field of 5 T. For this purpose, the flipping ratio R of the (0 1 2) reflection was measured as a function of time. In order to avoid the heating of the sample by the laser light, a chopped light experiment was carried out. The time evolution of $(1 - R)$ of the crystal under illumination by the laser at 2 K is shown in Figure 17.

The temperature dependence of the magnetisation induced by a field of 5 T ($\vec{H} // \vec{c}$) at 2 K in the photo-excited state of the $[\text{Fe}(\text{ptz})_6](\text{BF}_4)_2$ crystal was measured by PND and SQUID. A good agreement between the two techniques was found [36]. The relaxation of the photo-excited state towards the electronic stable state, due to thermal activation of the HS \rightarrow LS relaxation process, was observed in the 55–60 K temperature interval.

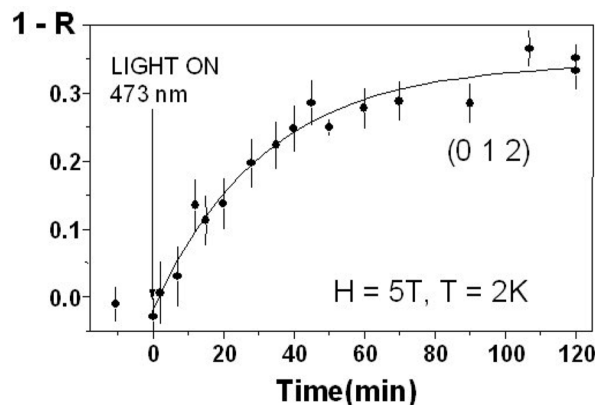


Figure 17. Kinetics of the photoexcitation process at 2 K, under 5 T using a radiation at 473 nm with power 30 mW.

The distribution of magnetisation density in the unit cell was reconstructed from 67 magnetic structure factors using a multipole model refinement. The radial expansion and the monopole population were refined for the iron and first neighbours nitrogen atoms and a goodness of fit GOF = 2.26 was obtained. The projection of the induced magnetisation density map along the crystallographic *c* axis is presented in Figure 18.

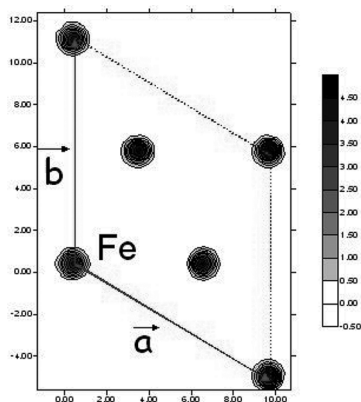


Figure 18. Induced magnetisation density map in the photoexcited state, at 2 K, under 5 Tesla, of the spin crossover compound $[\text{Fe}(\text{ptz})_6](\text{BF}_4)_2$, in projection along the *c* axis.

No significant density was observed in the refinement procedure on the nitrogen atoms ($0.03(8) \mu_B$). The moment of $4.05(7) \mu_B$ on the iron site is very close to the theoretical value of the Fe^{2+} moment at saturation ($S = 2$). This provides a direct evidence of the complete photo-transformation of the crystal.

This first determination of the magnetisation density in an excited state opens a new field of investigation in the field of photomagnetism. In charge transfer compounds where photoexcitation induces an electron transfer from a magnetic site towards another, modifying the local spin states, a direct evidence of this transfer mechanism could be provided by the magnetisation density study in the ground state and in the excited state.

8 ACKNOWLEDGEMENTS

The author thanks J. Schweizer, E. Ressouche and Y. Pontillon.

References

- [1] Kahn, O., in 'Molecular Magnetism', VVH Publishers, Inc., New York (1993).
- [2] Ferlay, S., Mallah, T., Ouahès, R., Veillet, P., Verdaguer, M., *Nature* **378** (1995) 701.
- [3] Delfs, C., Gatteschi, D., Pardi, L., Sessoli, R., Wieghard, K., Hanke, D., *Inorg. Chem.* **32** (1993) 3099.
- [4] Schweizer, J., in 'Introduction to physical techniques in molecular magnetism', Proc. of the Yesa Summer School, Ed. by Palacio, F., Ressouche, E., Schweizer, J., Zaragoza, 2000.
- [5] Bonnet, M., Delapalme, A., Becker, P., Fuess, H., *Acta Cryst. A* **32** (1976) 945.
- [6] Marshall, W., and Lovesey, S.W., *Theory of Thermal Neutron Scattering*, Oxford Univ. Press, Oxford 1971.
- [7] Ressouche, E., Thèse, Univ. Grenoble I (1991).
- [8] Forsyth, J.B., Wells, M., *Acta Cryst* **12** (1959) 412.
- [9] Squires G.L. in Introduction to the theory of thermal neutron scattering (Cambridge: University Press, 1978), p. 139.
- [10] Brown, P.J., Magnetic form factors, chapter 4.4.5, International tables for crystallography (1992) vol. C (A. J. C. Wilson, ed.), pp. 391–399.
- [11] Boucherle, J.X., Gillon, B., Maruani, J., Schweizer, J., *Mol. Phys.* **60** (1987) 1121.
- [12] Papoular, R., and Gillon, B., *Europhys. Lett.* **13** (1990) 429.
- [13] Schleger, P., Puig-Molina, A., Ressouche, E., Schweizer, J., *Acta Cryst. A* **53** (1997) 426.
- [14] Schweizer, J., Ressouche, E., in 'MagnetoScience D From Molecules to Materials', Eds Miller, J., Drillon, M., Wiley, (2001) pp. 325–355.
- [15] Brown, P.J., Capiomont, A., Gillon, B., Schweizer, J., *J. Mag. Mag. Mat.* **14** (1979) 289; Gillon, B., Thèse d'Etat, Univ. Pierre et Marie Curie, Paris (1983).
- [16] Hansen, N.K., and Coppens, P., *Acta Cryst A* **34** (1978) 909.
- [17] Clementi, E., and Raimondi, L.D., *J. Chem. Phys.* **38** (1963) 2686; Clementi, E. and Roetti, C., *Atomic Data and Nuclear Data Tables* **14** (1974) 177; Roetti, C. and Clementi, E., *J. Chem. Phys.* **60** (1974) 4725.
- [18] Holladay, A., Leung, P., Coppens, P., *Acta Cryst A* **39** (1983) 377.
- [19] Brown, J., Cambridge Crystallographic Subroutine Library (2006).
- [20] Kollmar, C., and Kahn, O., *Acc. Chem. Res.* **26** (1993) 259.
- [21] Schweizer, J., Gillon, B., in 'Magnetic properties of organic radicals', Ed. P.M. Lahti, Marcel Dekker, Inc., New York (1999) pp. 449–473.
- [22] Pontillon, Y., Bencini, A., Caneschi, A., Dei, A., Gatteschi, D., Gillon, B., Sangregorio, C., Stride, J., Totti, F., *Angew. Chem. Int. Ed.* **39** (2000) 1786.
- [23] Zheludev, A., Bonnet, M., Ressouche, E., Schweizer, J., Wan, M., Wang, H., *J. Mag. Mag. Mat.* **135** (1994) 147.
- [24] Romero, F.M., Ziessel, R., De Cian, A., Fischer, J., Turek, P., *New J. Chem.* **20** (1996) 919.
- [25] Romero, F.M., Ziessel, R., Bonnet, M., Pontillon, Y., Ressouche, E., Schweizer, J., Delley, B., Grand, A., Paulsen, C., *J. Am. Chem. Soc.* **122** (2000) 1298.
- [26] B. Gillon in 'MagnetoScience: From Molecules to Materials', Eds Miller, J., M. Drillon, Wiley, (2001) pp. 357–378.
- [27] Ressouche, E., Boucherle, J.X., Gillon, B., Rey, P., Schweizer, J., *J. Am. Chem. Soc.* **115** (1993) 3610.
- [28] Brown, P.J., Capiomont, A., Gillon, B., J. Schweizer, *Mol. Phys.* **48** (1983) 753.
- [29] Sikorav, S., Bkouche-Wacksman, I., Kahn, O., *Inorg. Chem.* **33** (1984) 490.

- [30] Thomson, L.K., Tandon, S.S., Manuel, M.E., *Inorg. Chem.* **34** (1995) 2356.
- [31] Aebersold, M.A., Gillon, B., Plantevin, O., Pardi, L., Kahn, O., Bergerat, P., von Seggern, I., Tuzek, F., Öhrström, L., Grand, A., Lelièvre-Berna, E., *J. Am. Chem. Soc.* **120** (1998) 5238.
- [32] Pontillon, Y., Caneschi, A., Gatteschi, D., Sessoli, R., Ressouche, E., Schweizer, J., Lelièvre-Berna, E., *J. Am. Chem. Soc.* **121** (1999) 5342.
- [33] Sangregorio, C., Gillon, B., Pontillon, Y., Ressouche, E., Sessoli, R., Caneschi, A., Gatteschi, D., to be published.
- [34] Sangregorio, C., Ohm, T., Paulsen, C., Sessoli, R., Gatteschi, D., *Phys. Rev. Lett.* **78** (1997) 4645.
- [35] Decurtins, S., Gütlich, P., Hasselbach, M.K., Spiering, H., Hauser, A., *Inorg. Chem.* **24** (1985) 2174.
- [36] Goujon, A., Gillon, B., Gukasov, A., Jftic, J., Nau, Q., Codjovi, E., F. Varret, *Phys. Rev. B* **67** (2003) 220401.

